Asian Journal of Pharmaceutical Sciences 19 (2024) 100925

Available online at www.sciencedirect.com

ScienceDirect

journal homepage: www.elsevier.com/locate/AJPS

Research Article

Immunotherapeutic hydrogel for co-delivery of STAT3 siRNA liposomes and lidocaine hydrochloride for postoperative comprehensive management of NSCLC in a single application

Xianglei Fu[a], *Yanbin Shi*[b], *Zili Gu*[c], *Hengchang Zang*[d], *Lian Li*[d], *Qingjie Wang*[e], *Yongjun Wang*[f], *Xiaogang Zhao*[g], *Hang Wu*[a], *Shengnan Qiu*[a], *Yankun Zhang*[a], *Jiamin Zhou*[a], *Xiangqin Chen*[a], *Hua Shen*[a], *Guimei Lin*[a,*]

[a] *Department of Pharmaceutics, School of Pharmaceutical Sciences, Cheeloo College of Medicine, Shandong University, Jinan 250012, China*
[b] *School of Mechanical and Automotive Engineering, Qilu University of Technology (Shandong Academy of Sciences), Jinan 250353, China*
[c] *Department of Radiology, Leiden University Medical Center, Albinusdreef 2, 2333 ZA Leiden, Netherlands*
[d] *NMPA Key Laboratory for Technology Research and Evaluation of Drug Products, School of Pharmaceutical Sciences, Cheeloo College of Medicine, Shandong University, Jinan 250012, China*
[e] *Laboratory of Basic Medical Sciences, Qilu Hospital, Shandong University, Jinan 250063, China*
[f] *Wuya College of Innovation, Shenyang Pharmaceutical University, Shenyang 110016, China*
[g] *Department of Thoracic Surgery, The Second Hospital of Shandong University, Jinan 250033, China*

ARTICLE INFO

Article history:
Received 14 September 2023
Revised 5 February 2024
Accepted 24 March 2024
Available online 3 May 2024

Keywords:
Liposome
Hydrogel
Signal transducer and activator of transcription 3
Non-small cell lung cancer
Macrophage

ABSTRACT

Despite standard treatment for non-small cell lung cancer (NSCLC) being surgical resection, cancer recurrence and complications, such as induction of malignant pleural effusion (MPE) and significant postoperative pain, usually result in treatment failure. In this study, an alginate-based hybrid hydrogel (SOG) is developed that can be injected into the resection surface of the lungs during surgery. Briefly, endoplasmic reticulum-modified liposomes (MSLs) pre-loaded with the signal transducer and activator of transcription 3 (STAT3) small interfering RNA and lidocaine hydrochloride are encapsulated in SOG. Once applied, MSLs strongly downregulated STAT3 expression in the tumor microenvironment, resulting in the apoptosis of lung cancer cells and polarization of tumor-associated macrophages towards the M1-like phenotype. Meanwhile, the release of lidocaine hydrochloride (LID) was beneficial for pain relief and natural killer cell activation. Our data demonstrated MSL@LID@SOG not only efficiently inhibited tumor growth but also potently improved the quality of life, including reduced MPE volume and pain relief in orthotopic NSCLC mouse models, even with a single administration. MSL@LID@SOG shows potential for

* Corresponding author.
E-mail address: guimeilin@sdu.edu.cn (G. Lin).
Peer review under responsibility of Shenyang Pharmaceutical University.

https://doi.org/10.1016/j.ajps.2024.100925

comprehensive clinical management upon tumor resection in NSCLC, and may alter the treatment paradigms for other cancers.

1. Introduction

Lung cancer is one of the leading causes of cancer-related deaths worldwide, where non-small cell lung cancer (NSCLC) accounts for >85% [1]. Surgical resection is the most effective treatment method for stages I–II and specific cases of stage IIIA of NSCLC [2]. However, the complex anatomy of NSCLC usually leads to inevitable local residual tumor micro-infiltration after resection, which leads to possible tumor recurrence and pleural metastasis. The malignant effusion in the pleural cavity (MPE) is normally observed together with pleural metastasis or surgery, which has profound immunosuppressive properties. These phenomena commonly cause dyspnea, presenting an enormous challenge in clinical patient management under the regulation of tumor-promoting myeloid immune cells [3,4]. The current standard of care for MPE includes catheter drainage or chemical and surgical pleurodesis, but it is largely palliative [5]. Recently, some researchers have been working on converting 'cold tumor' into 'hot tumor' in multiple ways, such as immune checkpoint blockade, pro-inflammatory cytokines application, and gene therapy [6,7]. Except for the insufficient antitumor effects, significant postoperative pain caused by thoracotomy or thoracoscopic approach also lowers the life quality of patients, especially in the first 48 h after surgery. In the clinic, it is advisable to employ locally multimodal analgesia to reduce complications [8]. Above all, the integrated management of antitumor recurrence, MPE reduction, and post-surgery pain relief is important in patients with NSCLC.

Signal transducer and activator of transcription 3 (STAT3) are important in NSCLC development, including angiogenesis, cell survival, cancer cell stemness, drug resistance, and evasion of antitumor immunity [9,10]. Because of the highly conserved domain and complex upstream signaling, antibodies or small-molecule inhibitors that effectively inhibit the STAT3 pathway are rare [11]. Inhibition of STAT3 by small interfering RNA (siRNA) is considered a promising anticancer strategy when sufficiently delivered to target sites [12]. It has been reported that liposomes are one of the most efficient systems for RNA delivery [13]. However, most of these vectors cannot avoid endosomal/lysosomal degradation, thus weakening the gene-silencing effects. In this regard, proper functionalization of nanoparticles to achieve precise subcellular targeting may be a promising strategy for protecting siRNA from degradation and improving activity *in vivo*. The introduction of intracellular membranes of eukaryotic organelles to the surface of nanoparticles, such as the endoplasmic reticulum (ER) and mitochondria membrane, are gradually being used for broader bio-interface functions [14,15].

Nowadays various systemically administered nanoparticles have been reported, whereas no more than 5% can access the tumor sites [16]. To avoid these limitations, local administration is applied during surgery and shows great potential for clinical application [17,18]. Hydrogels, as typical carriers used in local cancer treatment, have emerged in the last two decades for providing sustained release of payload and promoting penetration. The mechanical adhesion and stability of alginate hydrogels can be easily changed via compositional and structural modifications [19]. Additionally, they can be easily fabricated by various ligands via crosslink with calcium cations, such as sodium alginate (SA), which is a US Food and Drug Administration-approved material [18]. Therefore, it holds great potential in biomedical fields for delivering therapeutic agents when sprayed or injected onto complex anatomical surfaces.

In this study, we hypothesized that the co-delivery of lidocaine hydrochloride (LID) and STAT3 siRNA liposomes within a modified sodium alginate hydrogel (SOG) could inhibit local tumor recurrence after surgery and improve patient's quality of life by reducing MPE and relieving pain. Tumor treatment efficiency and immune responses were investigated *in vitro* and *in vivo*. Liposomes (MSLs) encapsulated siSTAT3 and modified with the ER membrane (EM) could deliver siRNA to both cancer and immune cells, influence the intracellular trafficking pathways, and enhance the silencing effects of siRNA. When SOG was loaded with MSLs and LID (MSL@LID@SOG), it could inhibit tumor growth without MPE development and improve the survival of mice. Compared with other immunotherapeutic hydrogel used in tumor treatment, this synergistic therapy based on SOG served as a release reservoir for multiple modulation therapies, enhanced the immune responses, and suppressed tumor-associated cytokines while reducing the adverse reactions that were associated with systemic drug exposure (Fig. 1). To the best of our knowledge, this is the first study on topical gel preparation for comprehensive management of NSCLC after surgery. This strategy may be clinically impactful and potentially offer a paradigm for other cancer types, such as ovarian carcinoma and mesothelioma.

2. Materials and methods

2.1. Materials

1,2-dioleoyl-3-trimethylammonium-propane (DOTAP) and 1,2-dioleoyl-sn-glycero-3-phoshoethanolamine (DOPE) were obtained from AVT Pharmaceutical Tech Co., Ltd. (Shanghai, China). Cholesterol and Endoplasmic Reticulum Isolation Kit were purchased from Sigma Aldrich (St Louis, USA). Sodium alginate, KIO_4, $CaCl_2$, and LID were bought from Shanghai

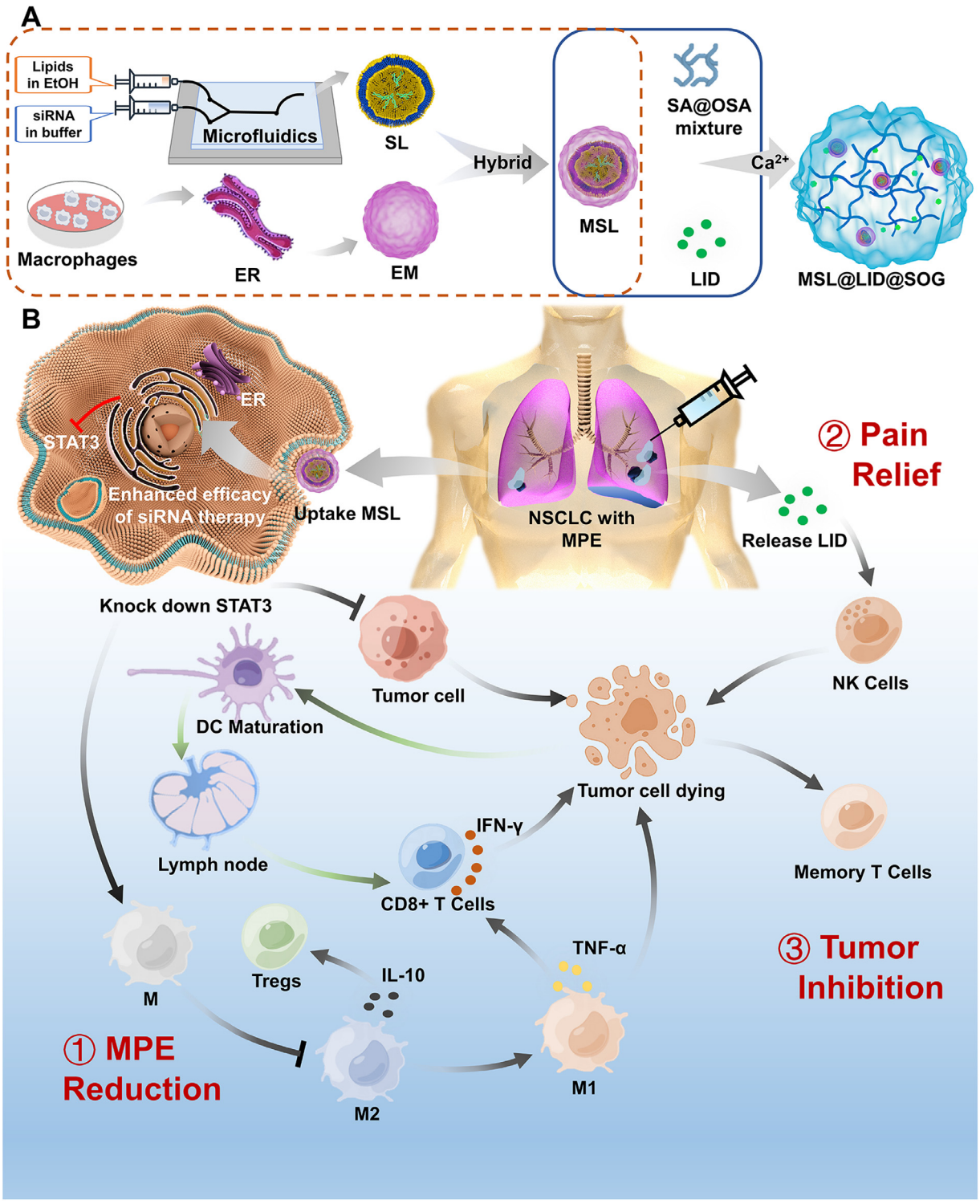

Fig. 1 – Schematic illustration of MSL@LID@SOG for NSCLC postoperative comprehensive management. (A) Schematic illustration to show the construction of MSL and hydrogel. (B) Diagram illustrating the brief mechanism of MSL@LID@SOG-mediated anticancer immunotherapy and multiple management effects. MSLs strongly downregulated STAT3 expression, resulting in the direct apoptosis of Lewis lung carcinoma cells, regulated the repolarization of M2-like macrophages, and promoted the activation of M1-like macrophages, thus accelerating the antitumor T cell responses and converting the cold immune microenvironment into the hot immune microenvironment. Meanwhile, the controlled release of LID in SOG is beneficial for pain relief and natural killer cell activation.

Aladdin Biochemical Technology Co., Ltd. (Shanghai, China). Other details were listed in the supporting information.

2.2. Preparation and characterization of MSLs

EM was prepared by the ER Isolation Kit (ER010) from RAW264.7 cells via ultracentrifugation. Liposomes were prepared by the film dispersion method or microfluidic mixing as previously described [20]. Specifically, they were constructed by mixing one volume of the ethanol phase containing lipids with 3 vol of siRNA in an aqueous phase in a microfluidic chip device, with the flow rate of 0.5 ml/min (ethanol) and 1.5 ml/min (aqueous buffer). The optimal formulation was confirmed by measuring the level of free siRNA in the supernatant after centrifugation (12,000 rpm for 10 min) via fluorescent dye-tagged assessment with nanodrop spectrophotometry or RiboGreen. Fluorescence-labeled SLs were prepared using the same method in the dark. Subsequently, siRNA-loaded liposomes (10 mg/ml) were mixed with EM solution (5 mg/ml) under ultrasonication for 1 min at 25 °C and extruded through 200 nm filters. The homogenous mixture was then dialyzed at 4 °C for purification.

The particle size distribution and zeta potential of the liposomes were analyzed on the Zetasizer Nano ZS system (Malvern, UK). The morphology of liposomes was observed via transmission electron microscopy (TEM, JEM 1200EX, JEOL, Japan).

After incubation with 10% serum at 37 °C for different periods, the samples were determined on a 1% agarose gel at 120 V for 15 min to evaluate the serum stability of MSLs. Sodium dodecyl sulfate-polyacrylamide gel electrophoresis analysis was performed to identify the protein profiles of EM and MSLs. Briefly, equal amounts of the total proteins from different samples were added to a 10% gel to separate proteins with different molecular weights and subsequently transferred onto polyvinylidene fluoride membranes. The membrane was stained with Coomassie blue G-250 for visualization.

2.3. Preparation and characterization of MSL@LID@SOG

According to the reported method, SA (0.5 g) and sodium periodate (0.5 g) were dissolved in deionized water and magnetically stirred in the dark for 5 h [21]. The reaction was terminated by adding ethylene glycol (0.75 ml), and the product was purified by dialysis for 72 h, followed by freeze-drying to obtain oxidized SA (OSA). The structure of the OSA (yield 82 %) was confirmed by Fourier transform infrared spectroscopy. To prepare the gel, 20 mg/ml SA solution pre-mixed with OSA at varying ratios was incubated with MSL (20 μg of siRNA per mg of alginate) and LID (405 μg of LID per mg of alginate) at 4 °C for 1 h. One ml of the resulting solution (20 mg alginate) was stirred with 50 μl of a 2 % calcium chloride solution for gelation studies.

The rheological behavior was evaluated using a rheometer (MCR302, Anton Par, Austria) with a shear rate range of 0–100 s^{-1} under a strain amplitude of 0.2%. Meanwhile, a 2-min dynamic sweep experiment was carried out under the constant angular frequency of 6 rad/s and 0.2% strain, after which the samples were subjected to 200% shear for 120 s (at a frequency of 6 rad/s) followed by a 2-min dynamic time sweep to evaluate the recovery ability of the gel after shape deformation. In addition, dye-loaded SOG was injected onto the surface of lungs isolated from New Zealand rabbits. The lungs were then allowed to inflate gradually by insufflation of air to achieve lung expansion. The area and *in vitro* bio-adhesive properties of the gels were monitored during this process. In addition, the 2% (v/v) red blood cell suspension isolated from fresh rabbit blood was incubated with the SOG hydrogel for the hemolysis assay. The absorbance of the supernatant after centrifugation was measured at 540 nm wavelength.

To characterize the microstructure of the gel, the composite hydrogel was lyophilized and observed via scanning electron microscopy (SEM, JSM-7500 F, JEOL, Japan). Gravimetric measurements were performed to evaluate the swelling behavior of the hydrogels. The weight of 500 μl hydrogel was recorded as W_0 and 5 ml of phosphate-buffered saline (PBS) was added to swell at 37 °C. The weights of the swollen hydrogels at different times were recorded as W_t. The relative swelling ratio (RSR) was calculated according to the following equation:

$$\text{RSR}\ (\%) = \frac{W_t - W_0}{W_0} \times 100\%$$

The release behavior of LID in the composite hydrogel was evaluated as follows: 1 ml of hydrogel was incubated with 10 ml release medium (PBS, pH 7.4 and 6.5) at 37 °C. For the release of MSLs characterization of the hydrogel, the Cy5-labeled siRNA MSLs were formulated with hydrogel and they were immersed in PBS. At predetermined time points, the released medium samples were withdrawn and replaced with fresh medium. The released LID was determined using high-performance liquid chromatography and the fluorescence intensity of released siRNA was measured by a fluorescence plate reader.

2.4. Uptake profile of MSLs in vivo

SOG with a total of 20 μg Cy5-labeled MSL, Cy5-labeled MSL and free siRNA were intrathoracically injected in the orthotopic NSCLC model. A small animal living imaging system (IVIS Spectrum, PerkinElmer) was used to obtain real-time images to determine the degradation and distribution of Cy5-siRNA after administration. Some animals were euthanized 24 h post-injection after MPE collection, and a flow cytometer was used to verify the uptake of MSLs *in vivo*. After incubation with red blood cell (RBC) lysis solution, single-cell suspensions from MPE were stained with anti-CD45, anti-CD3, and anti-F4/80. Only live cells (as determined by FVS700 staining) were gated for the analysis. Tumors in the lung tissues were frozen and prepared for immunofluorescence staining. Nuclei were stained with DAPI and macrophage staining was performed using anti-F4/80. Then, the confocal microscope (D-ECLIPSE C1, Nikon) was used to take photos.

2.5. Uptake and endocytosis of MSLs in vitro

MSLs loaded with carboxyfluorescein (FAM)-labeled siRNA were used to monitor uptake in bone marrow-derived macrophages (BMDMs) and Lewis lung cancer (LLC) cells. Cells were cultured overnight in 12-well plates (Corning) and incubated with different complete media containing SL and MSL with the same concentration of FAM-labeled siRNA. After treatment for 2, 4 and 6 h, the cells were assayed by a high-speed confocal platform (Dragonfly 200, Andor Technology) and Flow cytometry (FACS Calibur, BD Biosciences) as previously described [22]. All experiments were independently repeated three times.

To investigate the endocytosis pathway, LLC cells were seeded in a 12-well plate (1×10^5 cells/well). After incubation with chlorpromazine (CPZ), genistein (GEN), amiloride (AMI), and methyl-β-cyclodextrin (M-βCD) for 30 min to block the different endocytic pathways, the medium was replaced and added with FAM-labeled MSL and SL. After 1 h, cells were collected and measured via flow cytometry (FACS Calibur, BD Biosciences).

To determine the intracellular distribution of nanoparticles, LLC cells were seeded in confocal dishes and incubated with different complete media containing FAM-labeled siRNA, SL, or MSL for 6 h. The cells were then treated with Hoechst 33342 and ER-Tracker (1:1,000 dilution; Abcam) for 30 min before imaging via the high-speed confocal platform (Dragonfly 200, Andor Technology). The fluorescence co-localization of the green and red signals was compared using ImageJ software v.8.0 and the Pearson's correlation coefficients were calculated by Fiji.

2.6. mRNA knockdown and STAT3 protein expression

STAT3 mRNA knockdown was evaluated at 24 h post-treatment in LLC cells and BMDMs, respectively. Total RNA was extracted from cell lysates using the RNA-Quick Purification Kit and was reverse transcribed using a cDNA synthesis kit. The SYBR RT-PCR kit was used for analysis on a LightCycler480 II instrument (Roche, Germany). The data were analyzed using the $2^{-\Delta\Delta CT}$ method. Complexes of commercial transfection agents (jetPEI) and siRNA (PS) were prepared according to the manufacturer's instructions and analyzed similarly. To validate the expression of STAT3 mRNA, different treatments were administered at a concentration of 10 nM siSTAT3 12 h after the initial seeding of cells in 6-well plates. After 2 d, total protein was extracted by lysing cells with RIPA buffer for 20 min on ice and then centrifuging to remove precipitation. The expression of STAT3 was determined via Western blotting.

2.7. LLC cell proliferation, cytotoxicity, and apoptosis assays in vitro

Cell proliferation was assessed using a cell counting kit (CCK)−8. LLC cells (8×10^3) were seeded overnight in a 96-well plate and cultured with various treatments or gel extract samples (MSL+LID, MSL, LID, free RNA, and PBS) for 48 h. After treatment, each well was added with 10 μl CCK-8, and incubated at 37 °C for 2 h. Then, the wavelength of the absorbance microplate reader (Infinite F50, Tecan) was set at 450 nm, and optical density (OD) was obtained. Relative cell viability (RCV) was calculated according to the following equation:

$$\text{RCV (\%)} = \frac{OD_{test} - OD_{blank}}{OD_{control} - OD_{blank}} \times 100\%$$

In addition, calcein AM staining and propidium iodide (PI) staining were performed to distinguish live and dead cells, which were observed using an inverted fluorescence microscope (DP80, Olympus, Japan). For the apoptosis assay, cells after different treatments for 48 h were gently digested, resuspended, incubated with an anti-annexin V antibody and PI, and immediately detected via flow cytometry (FACS Calibur, BD Biosciences).

2.8. Cell migration and invasion assays

The human umbilical vein endothelial cells (HUVECs) are typically used for wound-healing assay and transwell assay. Pretreated HUVECs with different treatments for 36 h were seeded in a 6-well plate overnight, and a scratch was made using a 200-μl pipette tip. After that, the cells were photographed at 0 h and 24 h. ImageJ software was used for statistical analysis. The relative migration area was calculated as follows:

$$\text{Relative migration area (\%)} = \frac{\text{scratch area}_{0h} - \text{scratch area}_{24h}}{\text{scratch area}_{0h}} \times 100\%$$

Meanwhile, 100 μl medium without serum and inducers containing pretreated HUVECs was added to the 24-well transwell upper chambers, while 600 μl culture medium with 20% FBS and 2% cytokine was added to the lower layer. After 24 h, cells on the lower surface of the transwell chamber membrane were fixed and stained according to the instructions of the Cell Migration and Invasion Stain Kit. Migratory cells were quantified in five random microscopic fields by Inverted Microscope (Nikon, Ti2-U).

2.9. Differentiation of BMDMs in vitro

BMDMs generated with the macrophage colony-stimulating factor (GM-CSF) were stimulated by adding IL-4 (20 ng/ml) and IL-13 (20 ng/ml) to induce M2-like polarization and by adding lipopolysaccharide (100 ng/ml) and interferon (IFN)-γ (10 ng/ml) to induce M1-like macrophage induction. After incubation with different samples, the cells were washed and collected for cytometric analysis. They were incubated with FcR blocking solution and stained with anti-CD45, CD11c, F4/80, CD206, and iNOS according to the manufacturer's advice.

2.10. Antitumor experiment in NSCLC orthotopic tumor model

Mice with the orthotopic tumor model after 7 d were intrapleurally injected with MSL@LID@SOG, MSL@SOG,

SL@SOG, LID@SOG, and empty SOG ($n = 5$). The concentrations of siRNA were 1 mg/kg. The weights of the mice were recorded every 3 d, and the euthanasia point was determined as a loss of more than 20% of peak weight or deterioration of physical condition. Tumor development was mediated by luciferase signals every 7 d by IVIS. After 14 d of administration, all mice were scanned using micro-CT imaging and monitored for the occurrence of pulmonary effusion using a multimode small animal ultrasound/photoacoustic imaging system. Mean lung density was automatically calculated using the micro-CT data processing workstation (PerkinElmer Quantum GX2, Japan). On Day 21, pleural fluid specimens from mice were obtained using thoracentesis. Blood was collected to obtain the serum, and mice were euthanized to collect the important tissues. After collection, the blood was placed in a sterile Eppendorf tube at 4 °C for at least 1 h and was then centrifuged at 3,500 rpm for 20 min. The upper layer of yellow liquid was then removed and centrifuged at 8,000 rpm for 5 min to obtain the serum. *Ex vivo* luciferase signal images of the lungs were taken on Day 21 for quantitative evaluation, the lung wet weight was measured, and the right inferior lung lobe was fixed for subsequent hematoxylin-eosin (HE) and immunohistochemical staining. The upper lobes of the left lung were collected and stored at −80 °C. The tumors on the lung tissue were collected for flow cytometry analysis, and detailed staining methods are described in the supporting information. All animal studies were approved and conducted by the Ethics Committee of Scientific Research of Cheeloo College of Medicine, Shandong University, China.

For immunofluorescence staining of the vasculature, anti-mouse CD31 (1:200 dilution; Abcam), and goat anti-rat Cy3 (1:800 dilution; Abcam) were used on paraffin-embedded sections (5 μm) of the lungs, according to the manufacturer's recommendations. ELISA kits were used to determine the level of IFN-γ, TNF-α, IL-6, and IL-10 in serum according to the manufacturer's instructions. The liver and kidney functions were evaluated by using commercially alanine aminotransferase, aspartate aminotransferase, and blood urea nitrogen kits.

2.11. *Tumor growth inhibition in subcutaneous tumor mouse models*

Subcutaneous LLC tumor-bearing mice were randomly divided into five groups ($n = 5$ in each group). When the average volume of tumors reached 200 mm^3, the mice were anesthetized, and 90% of the tumors were resected in a sterile environment. Meanwhile, MSL@LID@SOG, MSL@SOG, SL@SOG, LID@SOG, and SOG were administered into the surgical region. The concentrations of siRNA were 1 mg/kg, respectively. Tumor growth in the resection locations was monitored, and the weights were recorded every 3 d. The formula for calculating tumor volume is as follows: $V = \frac{L \times W^2}{2}$, where L is the longest diameter of the tumor, and W is the shortest diameter of the tumor. The postoperative pain was measured directly on the tumor resection using Von Frey filaments, and the values were recorded as the body withdrawal threshold after surgery. The animals were euthanized on Day 16. Five tumors in each group were used for flow cytometry as described previously, and the remaining organs were fixed for subsequent staining. Harvested tissues were embedded and cut into 5 μm sections, followed by HE, TUNEL, and Ki67 staining.

2.12. *Long-term tumor inhibition and memory T cell population analysis*

LLC subcutaneous tumor-bearing mice were randomly divided into two groups ($n = 9$). When tumors reached an average volume of 100 mm^3, mice were peritumorally administered empty SOG or MSL@LID@SOG. After 15 d, the mice were anesthetized, and 90% of the tumors were resected in a sterile environment. Mice survival ($n = 6$) was monitored for 60 d. When the tumor volumes exceeded 1,000 mm^3, mice were considered dead. 30 d after the operation, three mice from each group were sacrificed to analyze the memory T cell population in the blood. Cells were stained for anti-CD45, CD3, CD4, CD8, CD44, and CD62L to evaluate the number of effector memory T cells via flow cytometry.

2.13. *Statistical analysis*

Statistical analyses were performed using the GraphPad Prism 9.0 software. All results were presented as the mean ± standard deviation(SD). Statistical significance was set at $P < 0.05$. One-way analysis of variance and Tukey's or Dunnett's post-hoc tests were performed to compare more than two groups. Survival was analyzed using the Kaplan–Meier curve and the log-rank test.

3. Results and discussion

3.1. *Preparation and characterization of MSLs*

In MSLs, siRNA was fully complexed with the liposomes at a ratio (1:1:1) of DOTAP, DOPE and cholesterol as shown in Fig. 1A. The loading capacity was approximately 3.5 nmol siSTAT3 per mg of SLs. Subsequently, SLs were decorated with EM isolated from RAW264.7 macrophages by serial sonication and extrusion to obtain MSLs. After EM decoration, the hydrodynamic diameter of MSLs was determined to be 146.03 ± 5.35 nm, slightly larger than that of SLs (123.67 ± 4.55 nm) (Fig. 2A). MSLs (22.0 ± 2.27 mV) also demonstrated lower zeta potentials relative to SLs (41.80 ± 2.23 mV). TEM images showed their spherical morphology, further confirming the successful membrane decoration on the surface of MSLs (Fig. 2B). Additionally, siRNA protected by MSLs remained stable after incubation with serum (10%, v/v) for 48 h. Still, the free siRNA was completely degraded during the same period (Fig. 2C), indicating these MSLs were more stable under physiological conditions than free siRNA. The protein components retained in MSLs were consistent with the electrophoresis strips of EM, but no protein signal was detected in SLs (Fig. 2D), which confirmed the successful modification of the EM.

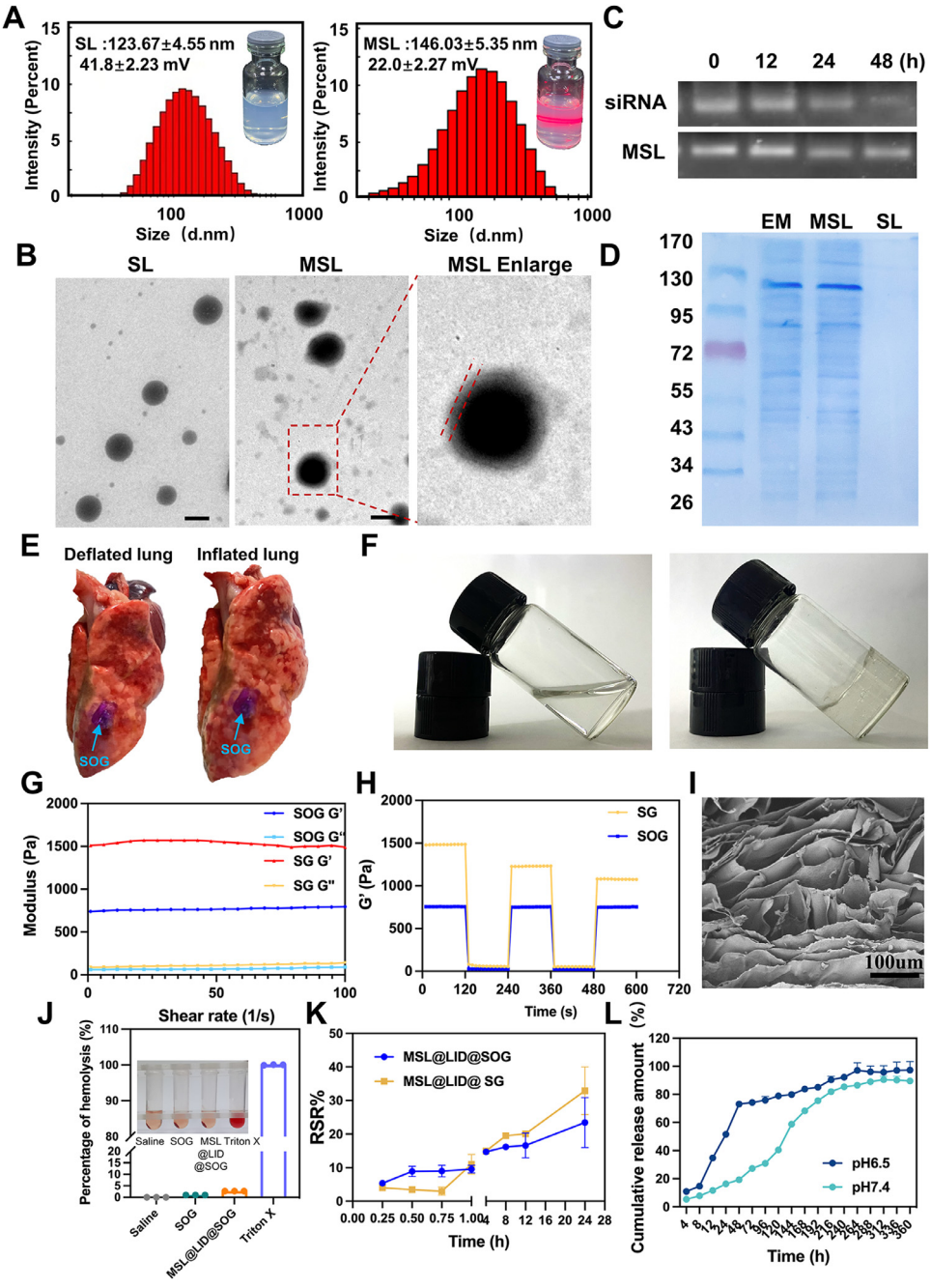

Fig. 2 – Construction and characterization of the MSL@LID@SOG. (A) Size distribution of SL and MSL. (B) Morphological images of SL and MSL, scale bar,100 μm. (C) MSL *in vitro* serum stability assessment by agarose gel electrophoresis. (D) Sodium dodecyl sulfate-polyacrylamide gel electrophoresis of membrane proteins. (E) Spread behavior of SOG during lung re-inflation. (F) Photographs of sol-to-gel transition after introducing Ca^{2+}. (G) Rheology properties of SOG, G', storage moduli, G'', loss moduli. (H) Storage moduli (G') under consecutive shear-thin/recovery cycles for 2 min. (I) Representative SEM images of SOG, scale bar,100 μm. (J) The hemolysis assay of MSL@LID@SOG ($n = 3$). (K) Changes in the relative swelling ratio of hydrogel in PBS at 37 °C ($n = 3$). (L) Release kinetics of LID from MSL@LID@SOG ($n = 3$). Data are shown as mean ± SD.

3.2. *Preparation and physical characterization of SOG*

Alginate has attracted attention due to its good biocompatibility, biodegradability, and mild gelation requirements [23,24]. In this study, hybrid hydrogels were prepared to balance their mechanical and self-healing properties, as previously reported [25]. OSA was first synthesized (Fig. S1), and fourier-transform infrared spectroscopy demonstrated the characteristic peak at 1732 cm^{-1} of the vibrational absorption of C=O bonds in the aldehyde groups (Fig. S2).

The formulation of SA–OSA hydrogels was studied by evaluating their tissue adhesion properties. The viscosity of the gel increased with an increase in the OSA percentage. When the proportion of OSA increased to 20%, the gel exhibited good adhesive activity with tissues, including the deflated and inflated lungs (Fig. 2E), which was attributed to Schiff base formation between the aldehyde group of OSA and the amino group of the tissue [26,27]. The gel was quickly formed after mixing with $CaCl_2$ (Fig. 2F), and the storage modulus (G′) was much greater than the loss modulus (G″), which is a typical feature of a viscoelastic gel (Fig. 2G). SOG displayed better shear recovery under multiple cycles of applied strain than SA gel (SG), which was more suitable for the diastolic and systolic rhythmicity features of the lungs (Fig. 2H). When SOG was delivered to the isolated lung, lung inflation was accompanied by the spread filling of SOG, as shown in Supplementary Video 1. SEM images of the gel confirmed that the porous network structure was uniformly distributed (Fig. 2I). Biocompatibility of the hydrogel was evaluated using a hemolysis test. As shown in Fig. 2J, the MSL@LID@SOG hydrogel (20 μg siSTAT3) caused negligible hemolysis. It also had an acceptable RSR with a maximum ratio of 23.42%, which was conducive to its prolonged existence in the tissue and stable drug release after swelling by the tissue fluid (Fig. 2K). Additionally, each ml of SOG was loaded with about 4 mg of LID and the loading efficiency of LID in the hydrogel was as high as 98.46% ± 0.45%. The release profiles of LID in PBS were studied *in vitro*. The gel exhibited a two-phase release as observed in Fig. 2L, including the burst release of 75% drugs within 48 h and the sustained release up to 15 d in the environment of pH 6.5. These typical release features of encapsulated therapeutic agents in hydrogels, with a gradually decreased release rate with time, exerted more potent therapeutic effects of LID, including quick pain relief after operation and long-term anticancer effects. These release profiles indicate that the release mechanism of LID was mainly driven by matrix dissolution and diffusion [28]. We also studied the release kinetics of siRNA from MSL@LID@SOG. The fluorescence intensity from the supernatant was measured by a fluorescence plate reader, and the results showed a sustained release for up to 2 weeks (Fig. S3).

3.3. In vivo *distribution and uptake of MSLs*

To investigate the distribution and uptake of MSLs *in vivo*, we examined the signal of CY5-labeled siSTAT3 in MSLs at different time points post-intrapleural injection of CY5-labeled MSL@SOG using the IVIS system. Intrapleural delivery resulted in the rapid increase of signal accumulation. Thereafter, the fluorescence signal from free siSTAT3 showed a rapid reduction. Liposomes ensured the presence of CY5-siRNA *in vivo* for up to 10 d, and further loading in SOG could keep the fluorescence signal of siRNA in the chest region up to 3 weeks after administration, whereas the free siSTAT3 signals only lasted for 3 d (Figs. 3A and S4). Although the fate of MSLs *in vivo* is complex, MSL@LID@SOG showed protective effects on the continuous release of siSTAT3.

We further explored the specific cellular internalization of CY5-labeled MSLs in the MPE of mice. CY5-labeled MSLs were mainly taken up by the $CD45^-$ cells which mainly consist of tumor-associated malignant cells (Fig. 3B) and $F4/80^+$ macrophages (Fig. 3C), whereas only a few MSLs were taken up by the $CD3^+$ T cells (Fig. 3D). Consistently, visualization assays of frozen lung sections revealed that MSLs colocalized with the $F4/80^+$ macrophages (Fig. 3E). The results obtained by frozen tumor section analysis showed that MSLs could increase the penetration of siRNA into the solid tumors (Fig. S5). Together, these data indicate that intrapleural MSL@LID@SOG facilitates the delivery of MSLs in both MPE and tumors.

3.4. In vitro *experiments on MSLs*

Since most of the MSLs were uptaken by LLC cells and BMDMs in the above experiments, we studied the intracellular fate of MSLs in these two cells *in vitro*. FAM-marked siRNA was used to understand the pathway of siSTAT3 delivery inside the cells. Fig. 3F and G showed that MSLs were effectively taken up by BMDMs and LLC cells *in vitro* after 2, 4, and 6 h of incubation in a time-dependent manner. Confocal laser scanning microscopy imaging results were consistent with this (Fig. S6 and S7). It has been reported that nanoparticles are normally taken up by cells in multiple ways, including endocytosis (*e.g.*, caveolin and clathrin) and micropinocytosis. From the internalization investigation in LLC cells, the endocytosis of MSLs was mediated by caveolin rather than clathrin (Fig. S8), which frequently bypasses endo-lysosomes and plays a critical role in cellular uptake and transcytosis [29].

The drug carrier can be directly transported to the ER or Golgi apparatus without passing through the lysosome after being internalized into cells through caveolin [30]. Since siRNA plays a role in gene interference in the ribosomes of ER, we performed the co-localization analysis of the ER and MSLs [31]. MSLs (green) and ER (red) merged in the same position, whereas the signal of SL was less prominent in the red position of the ER tracker (Fig. 3H). Pearson's correlation of MSLs ($r = 0.780$) was also much higher than SLs in the ER ($r = 0.427$). This increased transportation to the ER may be attributed to the function of EM-resident proteins in MSLs [32]. The effects of EM decoration on gene silencing of MSLs were further investigated. qPCR data showed that MSLs downregulated approximately 70% STAT3 expression in 10 nM siSTAT3 while free siRNA lost almost all activity (Fig. 3I). Such significant mRNA expression changes directly resulted in reduced protein expression as negligible protein bands were observed in MSLs (Fig. 3J). This inhibitory effect was two-fold higher than the commercial jetPEI reagents (PS).

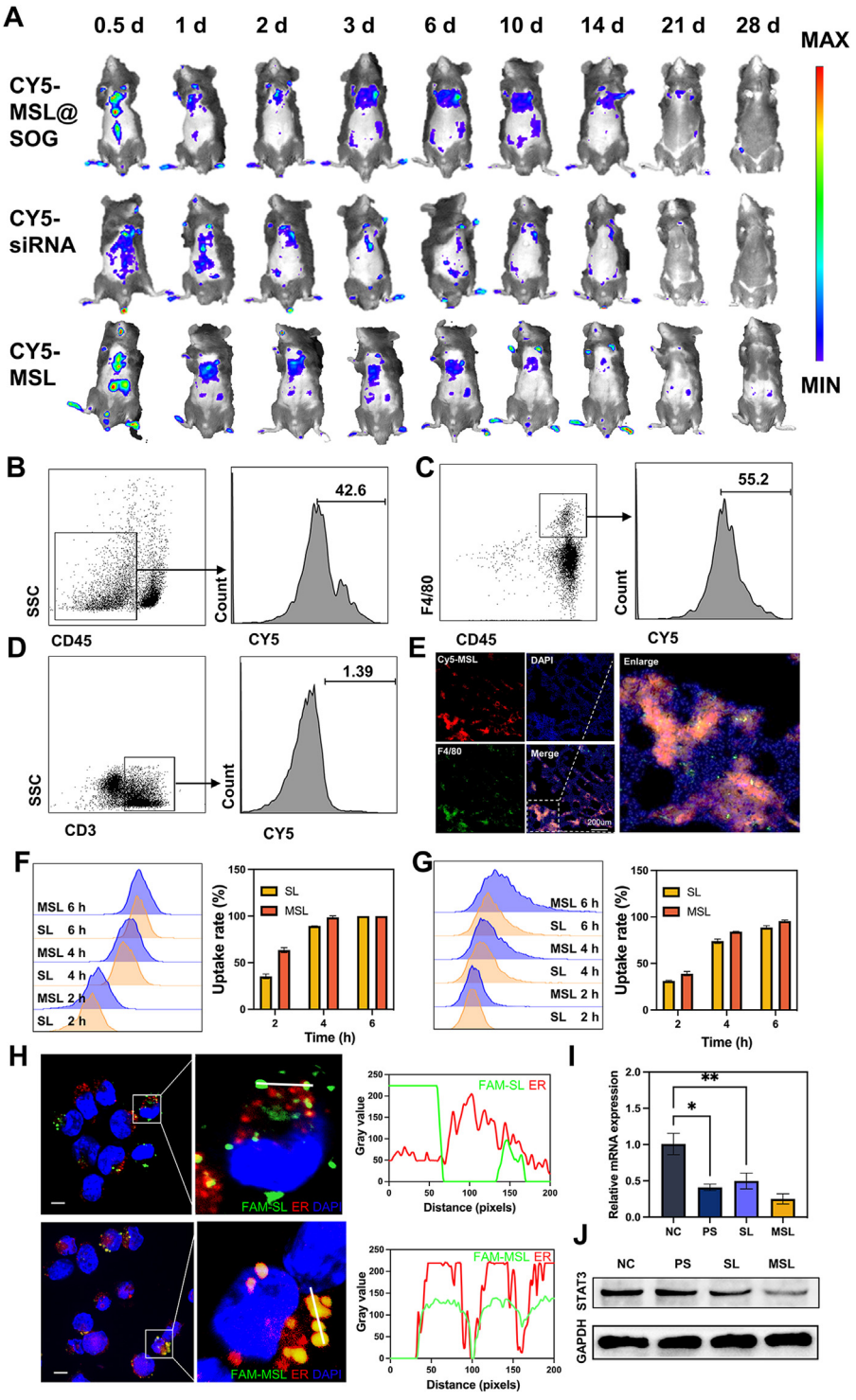

Fig. 3 – Biodistribution, uptake and subcellular localization of MSL *in vivo* and *in vitro*. (A) Biodistribution of intrapleurally injected CY5-labeled MSL@SOG in LLC model. (B-D) Mice with LLC models were intrapleurally injected with CY5-labeled MSLs. Representative flow cytometry of CY5-labeled MSL accumulation in CD45⁻cells, lymphocytes and macrophages in MPE. (E) Representative images of F4/80 immunofluorescent staining of frozen tumor sections, scale bar: 200 μm. (F-G) Flow cytometry analysis of FAM-labeled MSL and FAM-labeled SL internalized by BMDMs and LLC cells treated at 37 °C for 2, 4 and 6 h ($n = 3$ independent experiments). (H) Representative co-localization pictures of FAM-labeled MSL and FAM-labeled SL in ER, scale bar: 10 μm. (I) Relative STAT3 mRNA expression in the LLC cells treated by MSL (10 μM siRNA); *$P < 0.05$, **$P < 0.01$. (J) Expression levels of STAT3 protein treated by MSL in the LLC cells.

Furthermore, STAT3 of macrophages was also interfered by MSLs, both the mRNA and protein levels (Fig. S9 and S10). Based on these results, we speculated that the introduction of EM affected the intracellular trafficking of MSLs, prevented their degradation, and improved the gene-silencing effects of siSTAT3.

To study the cytotoxicity of MSLs and LID in the hydrogel, we added a concentration gradient of MSL and LID to the LLC cell culture medium with free siSTAT3 as a control. The half-maximal inhibitory concentration (IC_{50}) of MSLs+LID and MSLs was 17.93 and 21.20 nM, respectively (Fig. 4A). SOG gel extracts had good biocompatibility (Fig. S11). Based on the results of the gene silencing and cytotoxicity, we chose 20 nM as the ideal siSTAT3 concentration and 19.6 μM as the LID concentration for subsequent *in vitro* experiments. The cytotoxicity of different preparations was more intuitively demonstrated by calcein-AM and PI staining (Fig. S12). Fig. 4B showed that the MSL+LID (17.27% ± 0.90%) and MSL (13.73% ± 0.31%) groups induced significantly more apoptosis at 48 h than the PBS group.

After tumor removal, endothelial cell interactions, pleural invasion, and MPE production may trigger angiogenic effects and result in the first peak of early tumor relapse [33]. Therefore, we studied the effects of MSLs and LID on the invasion and migration of HUVECs. In the scratch wound healing assay, supplementation of MSLs and LID decreased the directional migration of HUVECs (Figs. 4C and S13). Representative images of HUVEC invasion following various stimulations are shown in Fig. 4D. Quantitatively, HUVEC invasion was significantly reduced in the MSL+LID group than in the basal control group (Fig. 4E). These data implied the role of the combination of siSTAT3 and LID in preventing postoperative metastases.

Next, we investigated the impact of MSL and LID on macrophage polarization. Macrophages were extracted from the mouse bone marrow and GM-CSF was added for repolarization (Fig. 4F). Notably, MSL@LID and MSLs containing 20 nM siSTAT3 did not induce obvious apoptosis in BMDMs (Fig. S14). The results showed that MSL+LID, MSL, and LID groups significantly manipulated the M1-like type polarization ($CD45^+$ $CD11b^+F4/80^+$ $iNOS^+$), while decreasing the differentiation to M2-like macrophages ($CD45^+$ $CD11b^+$ $F4/80^+$ $CD206^+$) (Fig 4G-4H).

3.5. In vivo *antitumor efficacy of MSL@LID@SOG in NSCLC orthotopic tumor models*

To investigate the potential effect of MSL@LID@SOG on antitumor in mice, a clinically orthotopic NSCLC mouse model was established using luciferase stably transfected with LLC cells (LLC-Luc) in C57BL/6 mice (Fig. 5A). After different treatments, we found increased weights of mice and survival in MSL@LID@SOG group, whereas 80% of mice died within 18 d post-challenge in the SOG group (Fig 5B–5C). Luciferase activity in LLC cells demonstrated that MSL@LID@SOG successfully eradicated the tumor on Day 14 and did not relapse until Day 21 (Fig. 5D). Assessment of the treatment effects by IVIS (Fig. 5E) and *ex vivo* examinations of lung tumor foci (Fig. 5G) showed that a single injection of MSL@LID@SOG significantly reduced the tumor burden, compared with SOG group. The results from weights and histology (Fig. 5F and 5G) further confirmed more potent antitumor effects of MSL@LID@SOG through lower lung wet weight and less necrosis. Meanwhile, the diffuse distribution of shadows in the micro-CT images of the lungs in the SOG group was contrasted with the clear textural features in the MSL@LID@SOG group (Fig. 5H). The control group showed an increased mean density, while treatment groups remained stable (Fig. 5J), and the combination treatment resulted in a further decrease in MPE volume (Fig. 5I). These data together suggest an impressive improvement in respiratory function and a greatly increased quality of life. Furthermore, the reduction of tumor cells in pleural effusion samples post-treatment was observed by optical microscopy (Fig. 5K). FACS analysis also showed a significant reduction in the number of $CD45^-$ cells, indicating the elimination of tumor cells after treatment (Fig. 5L). Last but not least, we also verified no significant harm to liver and kidney function by serum biochemical tests, which proved the safety of the treatment administered (Table S1).

Triggered by the anti-angiogenesis effects observed *in vitro*, we also confirmed this *in vivo* by staining vessels within lung tumors with anti-CD31 antibody. In contrast to the vasodilation and distortion observed with the SOG control, either MSL alone or in combination resulted in lower density of blood vessels (Fig. S15). The result suggested the role of the combination of siSTAT3 and LID in preventing postoperative recurrent metastasis.

3.6. *Immune response mediated by MSL@LID@SOG*

The excellent treatment efficacy in orthotopic NSCLC and MPE mouse models inspired us to explore whether MSL@LID@SOG treatment affected the immune infiltrates as shown in Fig. 6A. It has been demonstrated that macrophages account for more than half of all cells in the pleural cavity and play important roles in MPE development [34,35]. Encouraged by the *in vivo* uptake results of MSLs, we first examined the level of M1 and M2 subtype macrophages after MSL@LID@SOG treatment. In MPE, the proportion of M2-like macrophages, which protect cancer cells from apoptosis, was decreased in the MSL@LID@SOG group (Fig. 6B), and M1-like macrophages were rarely detected in MPE. Similarly, the number of M2-like macrophages in the lung tissue decreased upon MSL@LID@SOG treatment (Fig. 6C). It is noteworthy that the frequency of pro-inflammatory M1-like macrophages in the lung increased in comparison to the SOG control (Fig. 6D).

Many studies have linked tumor-infiltrating lymphocytes (TILs) with improved cancer outcomes, which overcome tumors' heterogeneity and immune escape [36]. In this study, we found our treatment caused an increase of $CD8^+$ T cells in tumor tissues (Fig. 6E), while the percentage of regulatory T cells (T_{regs}) ($CD25^+Foxp3^+$) was significantly decreased compared to control (Fig. 6F). Together with the infiltration of TILs, the highest increase of NK cells was also observed in the MSL@LID@SOG group, which may be attributed to the existence of LID (Fig. 6G) [37]. In addition, we found that this potent recruitment of cytotoxic T cells is also associated with the activation of DC, which was a prerequisite to initiating antitumor immunity. More activated

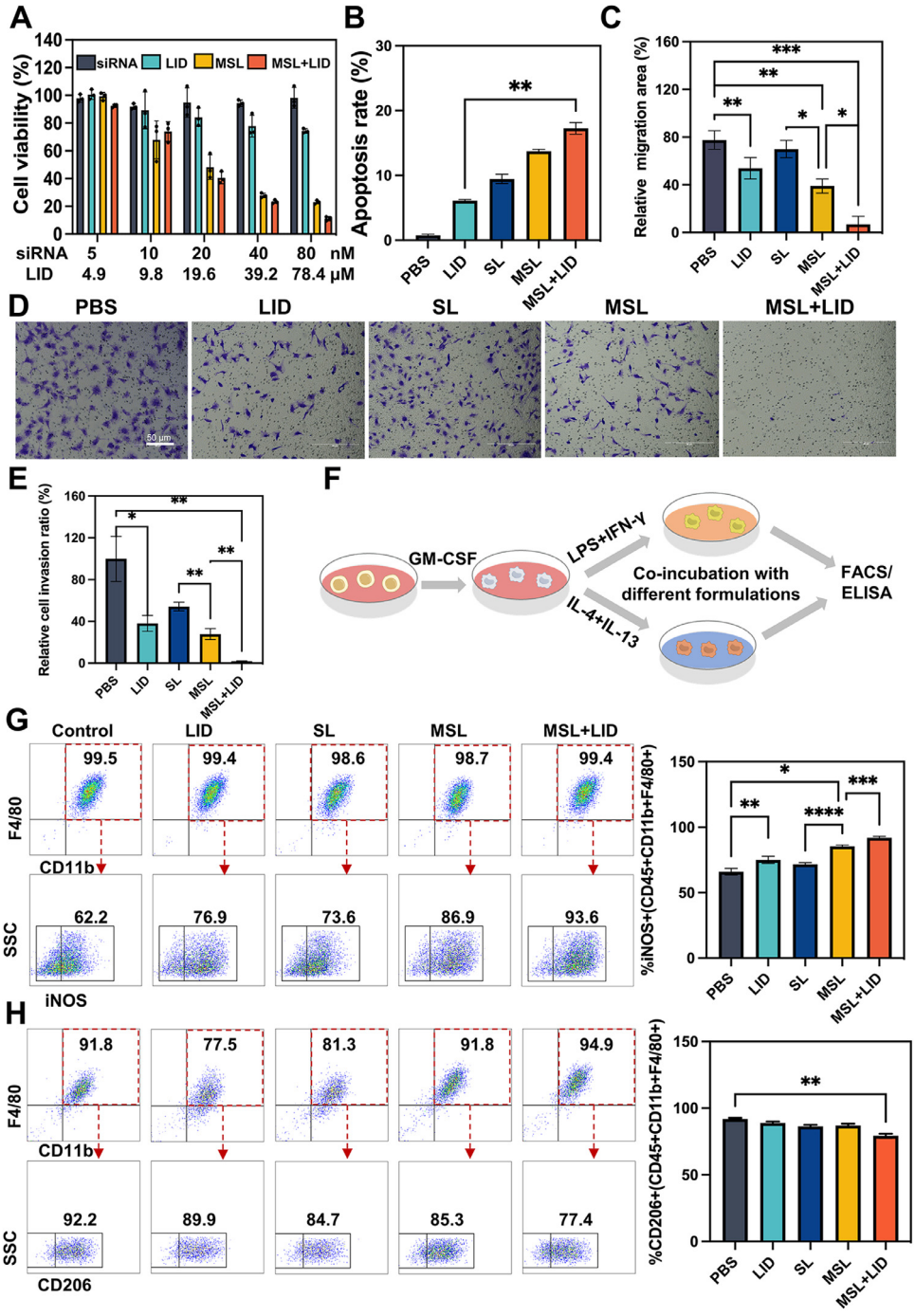

Fig. 4 – *In vitro* cytotoxicity, cell apoptosis assay, cell invasion assay and macrophage polarization induced by MSL and LID at the cellular level. (A) Cell viability of LLC cells after incubation with siRNA, LID and MSL for 48 h ($n = 3$). (B) The apoptosis rate of LLC cells after incubation with different preparations for 48 h by flow cytometry ($n = 3$). (C) Relative cell migration area of HUVECs after different treatments ($n = 3$). (D) Representative images and (E) quantitative results of HUVEC invasion after different treatments, scale bar: 50um ($n = 5$). (F) Schematic representation of BMDMs activation and polarization. (G-H) Effects on the polarized M1-like and M2-like macrophages after MSL and LID treatment. Quantification of the proportion of (G) M1-like and (H) M2-like macrophages after different treatments ($n = 4$). B, C, G and H were calculated by one-way ANOVA. *P < 0.05, **P < 0.01, ***P < 0.001, and ****P < 0.0001.

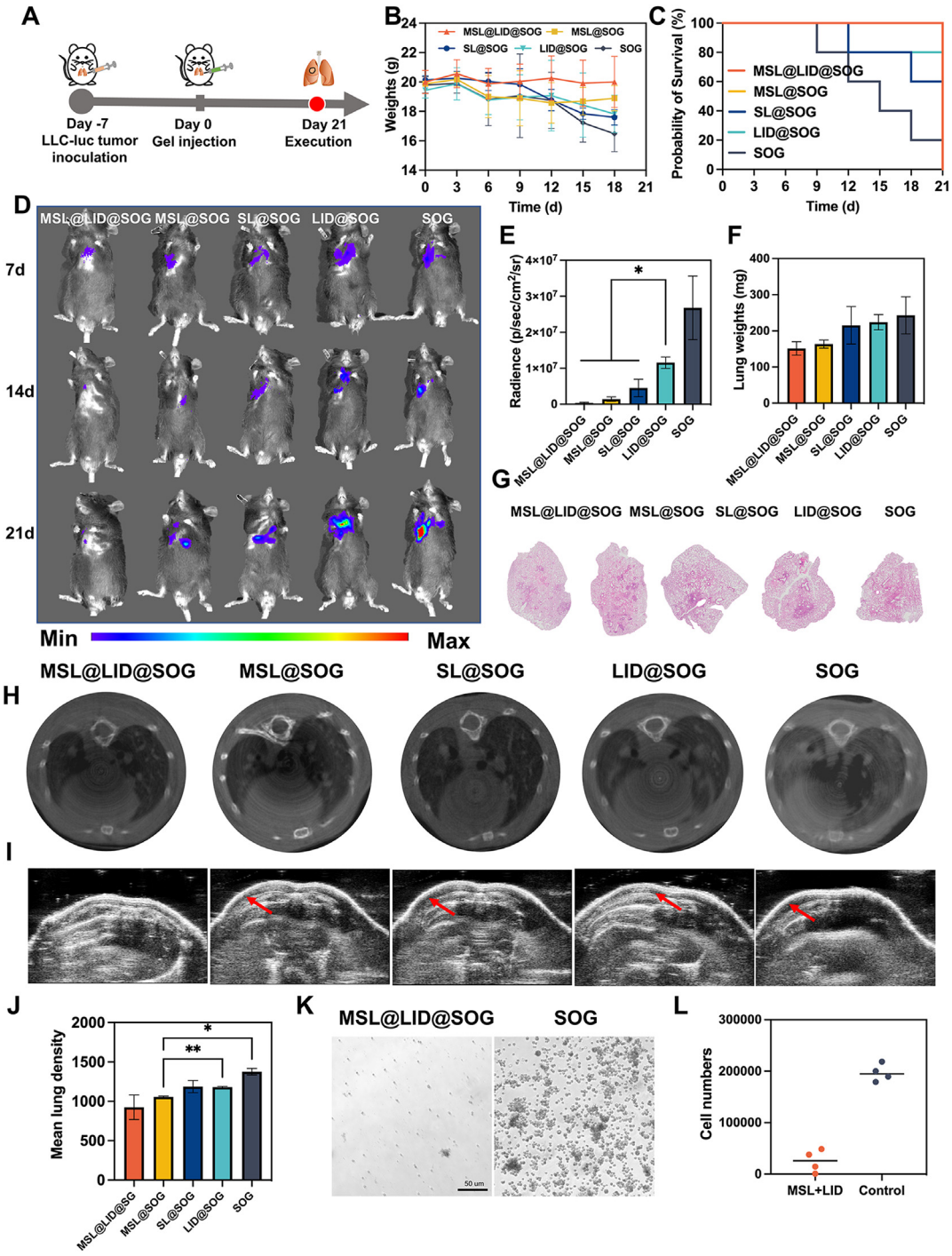

Fig. 5 – Anticancer efficacy of MSL@LID@SOG in orthotopic LLC model of mice. (A) Schematic diagram of the experimental treatment design in orthotopic LLC model. Intrathoracic injections of 5 x 10^5 LLC-luc cells were used to establish the orthotopic lung cancer model and induce the production of MPE. After 7 d, mice were intrapleurally injected with MSL@LID@SOG, MSL@SOG, SL@SOG, LID@SOG, and empty SOG (n = 5). Mice were sacrificed on Day 21 (n = 5). (B) Change curves of mice weights (n = 5). (C) Survival curves of mice in different groups (n = 5). (D) *In vivo* bioluminescence imaging of LLC tumor in mice and (E) statistical analysis of ROI in pleural tissues (n = 3). (F) Wet weights of the isolated lung after treatments (n = 3). (G) Representative HE sections of isolated lung. (H) Micro-CT imaging of mice thorax after various treatments on Day 14. (I) Representative ultrasonograph of mice showing MPE occurrence. (J) The mean lung tissue density after various treatments analyzed by Micro-CT imaging (n = 3). (K) Representative photographs and (L) $CD45^-$ cell numbers of MPE sampled from the thorax at Day 21, scale bar: 50 μm. Data are presented as mean ± SD; B, E, F and J were calculated via one-way ANOVA with a Tukey post hoc test, and C was analyzed by log-rank (Mantel-Cox) test; *$P < 0.05$, **$P < 0.01$.

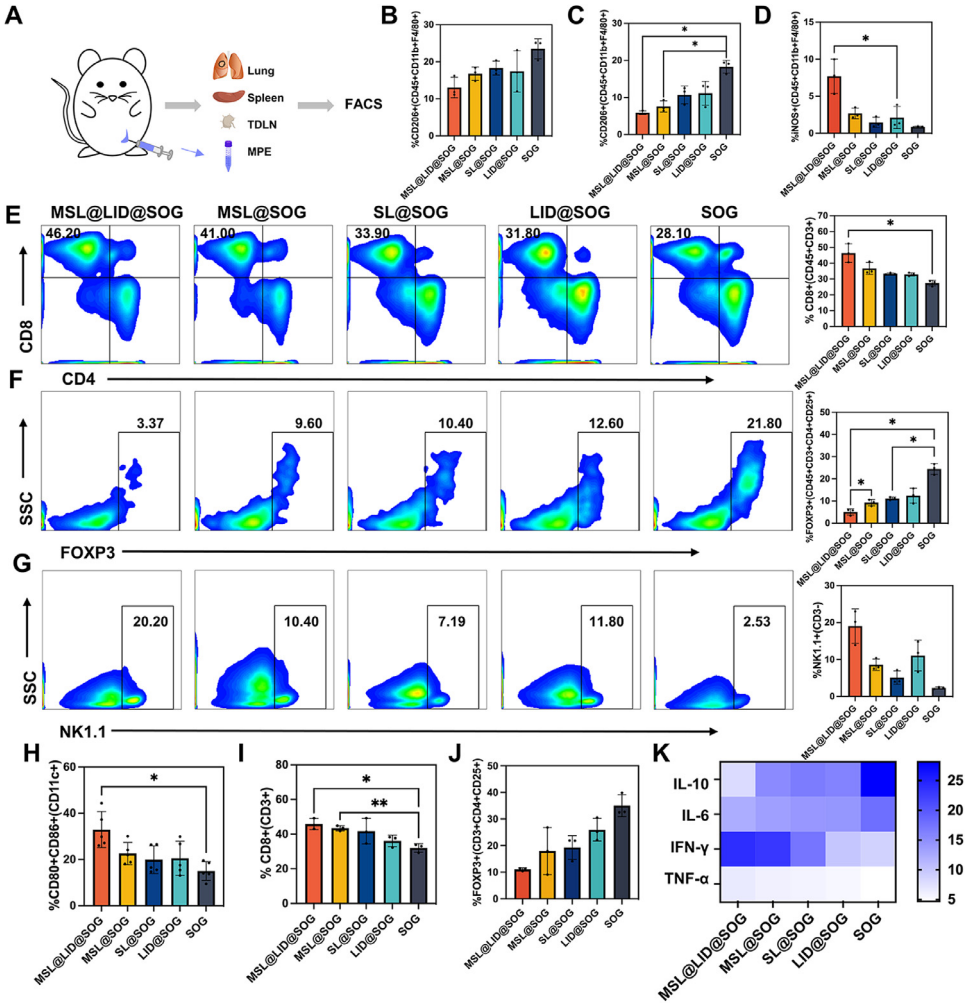

Fig. 6 – Antitumor immune response induced by MSL@LID@SOG in orthotopic LLC model. (A) Schematic diagram of the flow cytometric analysis of important organs. (B) Flow cytometry analysis of M2 cells in MPE ($n = 3$). (C) The quantitative analysis of M2-like cells ($CD45^+CD11b^+F4/80^+CD206^+$) and (D) M1-like macrophages ($CD45^+CD11b^+F4/80^+iNOS^+$) in lung tissues. (E) Flow cytometry analysis and the quantitative analysis of $CD45^+CD3^+CD8^+$T cells in tumors. (F) Number of Tregs ($CD45^+CD4^+CD25^+Foxp3^+$) and (G) NK cells ($CD45^+CD3^-NK1.1^+$) in tumors ($n = 3$). (H) Analysis of mature DCs ($CD11c^+CD80^+CD86^+$) in the lymph nodes ($n = 5$). (I) The quantitative analysis of $CD3^+CD8^+$T cells and (J) Tregs ($CD3^+CD4^+CD25^+Foxp3^+$) in spleens ($n = 3$). (K) Relative cytokine levels (TNF-α, IL-6, IL-10, and IFN-γ) in serum ($n = 5$). Data are presented as mean ± SD and were calculated via one-way ANOVA with a Tukey post hoc test. *$P < 0.05$ and **$P < 0.01$.

DC ($CD11c^+CD80^+CD86^+$) in tumor-draining lymph nodes were found in the MSL@LID@SOG group (Fig. 6H). Triggered by this potent local immune response, we sought to explore the systemic anticancer immune response by analyzing the level of lymphocytes in the spleen. Notably, a similar tendency was exhibited (Fig. 6I-J) and therefore indicated the strong systemic immune response induced by the combination treatment.

Besides, immune activation is a complex and multidimensional process that is controlled by intertwined regulatory signals, cytokines, and chemokines [38]. We also investigated the level of cytokine involved in antitumor immunity. ELISA revealed high levels of IFN-γ and TNF-α in serum, which synergized to induce tumor cell apoptosis. Low levels of IL-10 and IL-6 were also found in the serum after treatment (Fig. 6K), which was crucial for the antitumor immunity for lifted immune suppression. Taken together, these results indicated the potent immune response elicited by our combinational strategy, which partially explained the mechanism of the efficient antitumor effects.

3.7. In vivo *antitumor efficacy of MSL@LID@SOG in other tumor models*

Then, we used an incomplete tumor resection model to validate the therapeutic effects of MSL@LID@SOG. LLC subcutaneous tumor-bearing mice were randomly divided into five treatment groups and administered with different formulations in the surgical region (Fig. 7A). Generally, the body weights of the mice were not affected by treatment (Fig. 7C). HE staining did not detect any significant inflammation in important organs (Fig. S16), suggesting

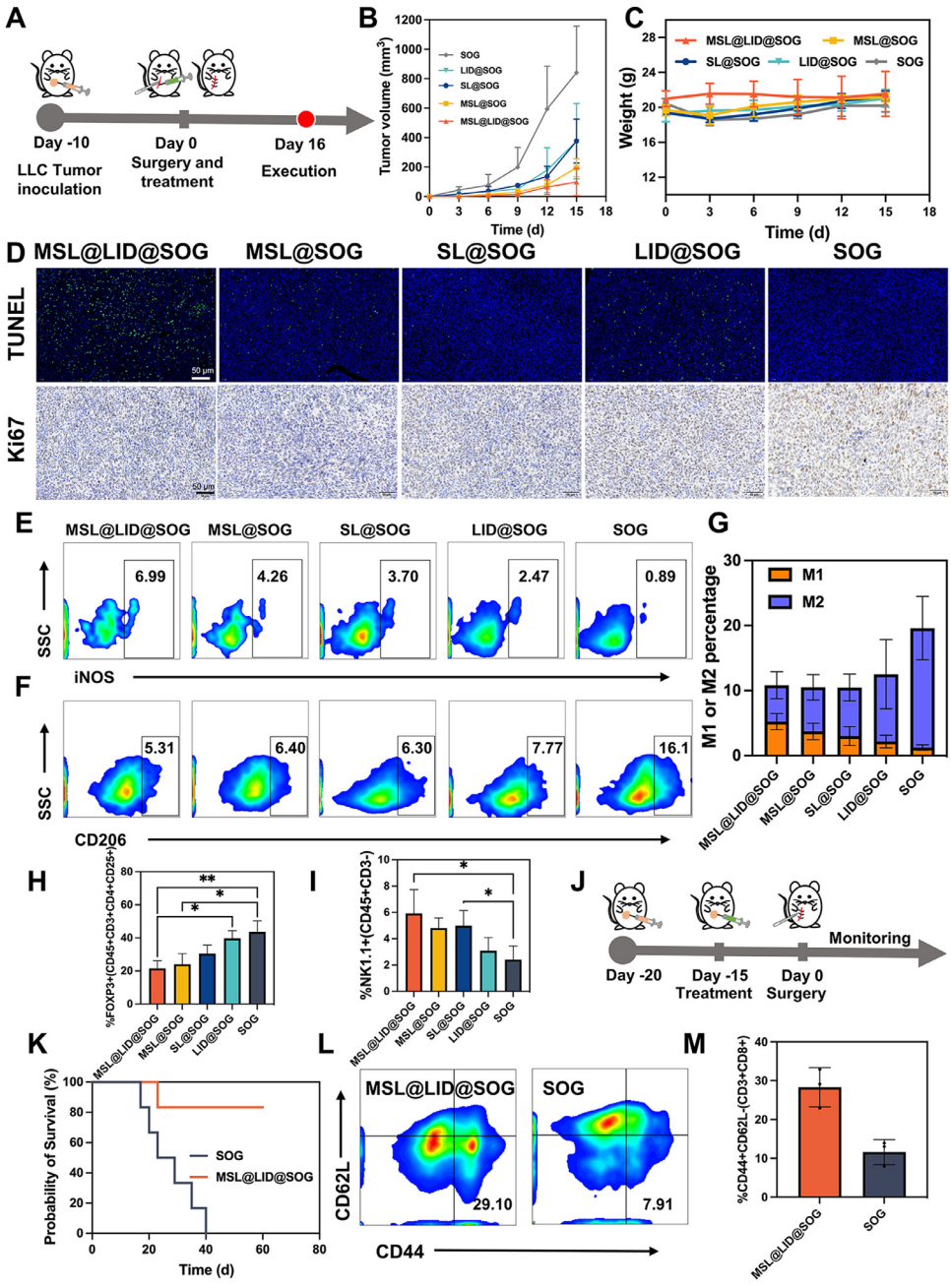

Fig. 7 – Anticancer efficacy of MSL@LID@SOG in incomplete tumor resection model. (A) Schematic illustration of the experimental treatment design in subcutaneous LLC model. LLC cells (1 x 10^6) were subcutaneously injected into the right side of each C57BL/6. When tumors reached an average volume of ~200 mm^3, mice were anesthetized and 90 % of tumors were resected. Meanwhile, five different formulations were administered into the surgical region and the wound was sutured. Mice were euthanized on Day 16 (n = 5). (B) Curves showing tumor volumes of mice after various treatments (n = 5). (C) Change curves of mice weights after various treatments (n = 5). (D) TUNEL (apoptotic cell shown in green), and Ki67 immunohistochemistry (proliferative cells shown in brown) in tumor tissues from mice treated with MSL@LID@SOG. Scale bars are 50 μm. (E) Flow cytometry analysis of M1-like macrophages ($CD45^+CD11b^+F4/80^+iNOS^+$) and (F) M2-like cells ($CD45^+CD11b^+F4/80^+CD206^+$) and (G) their quantitative analysis in tumors (n = 5). (H) Number of Tregs ($CD45^+CD4^+CD25^+Foxp3^+$) and (I) NK cells ($CD45^+CD3^-NK1.1^+$) in the tumor (n = 5). (J) Schematic illustration of the experimental design in long-term antitumor treatments. (K) Mice survival rates in long-term antitumor treatments (n = 6). (L) Flow cytometry analysis and m statistical data of $CD8^+T_{EM}$ ($CD8^+CD44^+CD62L^-$) on Day 40 (n = 3). B, C and H–I were performed using a one-way ANOVA test; *P < 0.05, **P < 0.01.

the good safety of these treatments. Nevertheless, compared to the MSL@SOG and SOG groups, animals treated with MSL@LID@SOG and LID@SOG exhibited normal appearance (hair, eye, tail, etc.) and behaviors (feeding, drinking, and excretion) on the first 3 d after surgery, while mice in other groups suffered from moderate pain during this period. We have also used Von Frey filaments as quantitative sensory testing to assess hypersensitivity locally in the surgical wound area in postoperative mice. Results showed that LID in the hydrogel platforms was more effective as a painkiller in the first 3 d after surgery. The strongest bending force in MSL@LID@SOG group and LID@SOG group was about 12 g, and the threshold in other mice was 3 g (Fig. S17). After resection, MSL- and LID-treated tumors were significantly smaller than control-treated tumors at Day 9, while MSL@LID@SOG group showed the slightest tumor regrowth (Fig. 7B). Immunohistochemistry photos of tumors also demonstrated that the combination treatment induced a significantly higher apoptotic rate and limited proliferation (Fig. 7D). Moreover, although the infiltration of TILs was relatively less, the overall alterations in immune cells (M1, M2-like macrophages, NK cells, and T_{regs}) in subcutaneous tumors were consistent with the orthotopic tumors (Fig. 7E–I).

Except for the immediate immune response, long-term immune memory is important for the prevention of tumor recurrence and metastasis [39]. To evaluate the immune memory effect *in vivo*, LLC subcutaneous tumor-bearing mice were peritumorally administered different formulations, as illustrated in Fig. 7J. At Day 30 post treatment, the numbers of $CD8^+T_{EM}$ ($CD44^+CD62L^-$) were significantly increased in the MSL@LID@SOG group, compared to the control group (Fig 7L and 7M). And over 80% of mice ultimately survived for 60 d (Fig. 7K). This generation of immunological memory is the hallmark of effective and prolonged immunity, which is capable of providing long-term protection against tumor recurrence.

Based on these data, MSL@LID@SOG manipulates a local tumor into a state where the antitumor immune response is activated, and postoperative comprehensive management is offered (Fig. 1B). Upon injection, MSLs are taken up by both cancer and immune cells in the tumor. On the one hand, MSLs strongly downregulate STAT3 expression, resulting in direct apoptosis in tumor cells. The dying cells trigger the activation of DCs that migrate to tumor-draining lymph nodes and initiate antitumor immunity. On the other hand, the knockdown of STAT3 normalizes the immunosuppressive pathways in macrophages in a non-toxic way, which leads to the repolarization of anti-inflammatory M2-like macrophages towards the pro-inflammatory M1-like subtype. At the same time, multiple cytokines participate in the regulation of T cell proliferation and function, such as IFN-γ, TNF-α, IL-6, and IL-10, etc. Besides, except for pain relief, LID was also found to contribute to efficient NK cell expansion, thus enhancing NK cell-mediated cytotoxicity against tumor cells.

4. Conclusion

In summary, we developed a locally post-surgical hydrogel platform, which delivered MSLs capable of entering cells and released LID sustainably. MSL@LID@SOG induced a strong immune response, thereby maximizing the antitumor therapeutic efficacy. MSL-mediated inhibition of STAT3 elicited direct antitumor activity, enhanced the immune responses in the tumor microenvironment, and remodeled MPE. Meanwhile, the controlled release of LID in SOG was found to be beneficial for pain relief and NK cell activation. Overall, these results provide a practicable hydrogel system to inhibit tumor recurrence and prevent postoperative complications, which may be translated clinically in NSCLS as well as other cancer types. To this end, considerations about drug dosage, particle size, and pharmacokinetics in large animal models should also be addressed in the future.

Conflicts of interest

The authors declare no conflict of interest.

Acknowledgments

The authors acknowledge the Pharmaceutical Biology Sharing Platform and Translational Medicine Core Facility of Shandong University. The authors also thank the Laboratory of Basic Medical Sciences of Qilu Hospital, Shandong University. This work was supported by the National Natural Science Foundation of China [grant numbers 21873057, 22373059] and the Natural Science Foundation of Shandong Province [grant numbers ZR2023MB082].

Supplementary materials

Supplementary material associated with this article can be found, in the online version, at doi:10.1016/j.ajps.2024.100925.

References

[1] Siegel RL, Miller KD, Jemal A. Cancer statistics, 2020. CA Cancer J Clin 2020;70(1):7–30.
[2] Siegel RL, Miller KD, Fuchs HE, Jemal A. Cancer statistics, 2022. CA Cancer J Clin 2022;72(1):7–33.
[3] Murthy P, Ekeke CN, Russell KL, Butler SC, Wang Y, Luketich JD, et al. Making cold malignant pleural effusions hot: driving novel immunotherapies. Oncoimmunology 2019;8(4):e1554969.
[4] Guo M, Wu F, Hu G, Chen L, Xu J, Xu P, et al. Autologous tumor cell–derived microparticle-based targeted chemotherapy in lung cancer patients with malignant pleural effusion. Sci Transl Med 2019;11(474):eaat5690.
[5] Liu Y, Wang L, Song Q, Ali M, Crowe WN, Kucera GL, et al. Intrapleural nano-immunotherapy promotes innate and adaptive immune responses to enhance anti-PD-L1 therapy for malignant pleural effusion. Nat Nanotechnol 2022;17:206–16.
[6] Tseng YH, Ho HL, Lai CR, Luo YH, Tseng YC, Whang-Peng J, et al. PD-L1 expression of tumor cells, macrophages, and immune cells in non–small cell lung cancer patients with malignant pleural effusion. J Thorac Oncol 2018;13(3):447–53.

[7] Alley EW, Katz SI, Cengel KA, Simone CB. Immunotherapy and radiation therapy for malignant pleural mesothelioma. Transl Lung Cancer Res 2017;6(2):212–19.
[8] Feray S, Lubach J, Joshi GP, Bonnet F, Van de Velde M, Joshi GP, et al. PROSPECT guidelines for video-assisted thoracoscopic surgery: a systematic review and procedure-specific postoperative pain management recommendations. Anaesthesia 2022;77(3):311–25.
[9] Parakh S, Ernst M, Poh AR. Multicellular effects of stat3 in non-small cell lung cancer: mechanistic insights and therapeutic opportunities. Cancers 2021;13(24):6228.
[10] Busker S, Qian W, Haraldsson M, Espinosa B, Johansson L, Attarha S, et al. Irreversible TrxR1 inhibitors block STAT3 activity and induce cancer cell death. Sci Adv 2020;6(12):eaax7945.
[11] Henley MJ, Koehler AN. Advances in targeting 'undruggable' transcription factors with small molecules. Nat Rev Drug Discov 2021;20(9):669–88.
[12] Ngamcherdtrakul W, Reda M, Nelson MA, Wang R, Zaidan HY, Bejan DS, et al. *In situ* tumor vaccination with nanoparticle co-delivering CpG and STAT3 siRNA to effectively induce whole-body antitumor immune response. Adv Mater 2021;33(31):e2100628.
[13] Baltusnikas J, Fokin A, Winkler J, Liobikas J. Long-term regulation of gene expression in muscle cells by systemically delivered siRNA. J Control Release 2017;256:101–13.
[14] Qiu C, Han HH, Sun J, Zhang HT, Wei W, Cui SH, et al. Regulating intracellular fate of siRNA by endoplasmic reticulum membrane-decorated hybrid nanoplexes. Nat Commun 2019;10(1):2702.
[15] Gong H, Zhang Q, Komarla A, Wang S, Duan Y, Zhou Z, et al. Nanomaterial biointerfacing via mitochondrial membrane coating for targeted detoxification and molecular detection. Nano Lett 2021;21(6):2603–9.
[16] Chen Q, Wang C, Zhang X, Chen G, Hu Q, Li H, et al. In situ sprayed bioresponsive immunotherapeutic gel for post-surgical cancer treatment. Nat Nanotechnol 2019;14(1):89–97.
[17] Majumder P, Singh A, Wang Z, Dutta K, Pahwa R, Liang C, et al. Surface-fill hydrogel attenuates the oncogenic signature of complex anatomical surface cancer in a single application. Nat Nanotechnol 2021;16(11):1251–9.
[18] Wang F, Su H, Xu D, Dai W, Zhang W, Wang Z, et al. Tumour sensitization via the extended intratumoural release of a STING agonist and camptothecin from a self-assembled hydrogel. Nat Biomed Eng 2020;4(11):1090–101.
[19] Bauleth-Ramos T, Shih TY, Shahbazi MA, Najibi AJ, Mao AS, Liu D, et al. Acetalated dextran nanoparticles loaded into an injectable alginate cryogel for combined chemotherapy and cancer vaccination. Adv Funct Mater 2019;29(15):1903686.
[20] Qiu C, Han HH, Sun J, Zhang HT, Wei W, Cui SH, et al. Regulating intracellular fate of siRNA by endoplasmic reticulum membrane-decorated hybrid nanoplexes. Nat Commun 2019;10(1):2702.
[21] Zhang M, Qiao X, Han W, Jiang T, Liu F, Zhao X. Alginate-chitosan oligosaccharide-ZnO composite hydrogel for accelerating wound healing. Carbohydr Polym 2021;266:118100.
[22] Fu X, Shi Y, Zang H, Wang Q, Wang Y, Wu H, et al. Combination of oxaliplatin and POM-1 by nanoliposomes to reprogram the tumor immune microenvironment. J Control Release 2022;347:1–13.
[23] Tringides CM, Vachicouras N, de Lázaro I, Wang H, Trouillet A, Seo BR, et al. Viscoelastic surface electrode arrays to interface with viscoelastic tissues. Nat Nanotechnol 2021;16(9):1019–29.
[24] Qin J, Li M, Yuan M, Shi X, Song J, He Y, et al. Gallium(III)-mediated dual-cross-linked alginate hydrogels with antibacterial properties for promoting infected wound healing. ACS Appl Mater Interfaces 2022;14(19):22426–42.
[25] Wei Z, Yang JH, Liu ZQ, Xu F, Zhou JX, Zrínyi M, et al. Novel biocompatible polysaccharide-based self-healing hydrogel. Adv Funct Mater 2015;25(9):1352–9.
[26] Conde J, Oliva N, Zhang Y, Artzi N. Local triple-combination therapy results in tumour regression and prevents recurrence in a colon cancer model. Nat Mater 2016;15(10):1128–38.
[27] Mo X, Iwata H, Ikada Y. A tissue adhesives evaluated *in vitro* and *in vivo* analysis. J Biomed Mater Res A 2010;94(1):326–32.
[28] Ashley GW, Henise J, Reid R, Santi DV. Hydrogel drug delivery system with predictable and tunable drug release and degradation rates. Proc Natl Acad Sci USA 2013;110(6):2318–23.
[29] He W, Xing X, Wang X, Wu D, Wu W, Guo J, et al. Nanocarrier-mediated cytosolic delivery of biopharmaceuticals. Adv Funct Mater 2020;30(37):1910566.
[30] Yang C, He B, Dai W, Zhang H, Zheng Y, Wang X, et al. The role of caveolin-1 in the biofate and efficacy of anti-tumor drugs and their nano-drug delivery systems. Acta Pharm Sin B 2021;11(4):961–77.
[31] Tai W, Li J, Corey E, Gao X. A ribonucleoprotein octamer for targeted siRNA delivery. Nat Biomed Eng 2018;2(5):326–37.
[32] Shi Y, Wang S, Wu J, Jin X, You J. Pharmaceutical strategies for endoplasmic reticulum-targeting and their prospects of application. J Control Release 2021;329:337–52.
[33] Changchien CY, Chen Y, Chang HH, Chang SY, Tsai WC, Tsai HC, et al. Effect of malignant-associated pleural effusion on endothelial viability, motility and angiogenesis in lung cancer. Cancer Sci 2020;111(10):3747–58.
[34] Brambilla E, Le Teuff G, Marguet S, Lantuejoul S, Dunant A, Graziano S, et al. Prognostic effect of tumor lymphocytic infiltration in resectable non-small-cell lung cancer. J Clin Oncol 2016;34(11):1223–30.
[35] Song Z, Luo W, Zheng H, Zeng Y, Wang J, Chen T. Translational nanotherapeutics reprograms immune microenvironment in malignant pleural effusion of lung adenocarcinoma. Adv Healthc Mater 2021;10(12):e2100149.
[36] Wu H, Fu X, Zhai Y, Gao S, Yang X, Zhai G. Development of effective tumor vaccine strategies based on immune response cascade reactions. Adv Healthc Mater 2021;10(13):e2100299.
[37] Kim R. Effects of surgery and anesthetic choice on immunosuppression and cancer recurrence. J Transl Med 2018;16(1):8.
[38] Chao Y, Liu Z. Biomaterials tools to modulate the tumour microenvironment in immunotherapy. Nat Rev Bioengineering 2023;1:125–38.
[39] van Leent MMT, Priem B, Schrijver DP, de Dreu A, Hofstraat SRJ, Zwolsman R, et al. Regulating trained immunity with nanomedicine. Nat Rev Mater 2022;7:465–81.